Dynamic quantum state holography

K. Eickhoff, S. Kerbstadt, T. Bayer, and M. Wollenhaupt
Institut für Physik, Carl von Ossietzky Universität Oldenburg, Carl-von-Ossietzky-Straße 9-11, 26129 Oldenburg, Germany

(Received 28 October 2019; published 27 January 2020)

We present a pulse-shaper-based holographic technique for the time-resolved and phase-sensitive observation of ultrafast quantum dynamics. The technique combines bichromatic white light polarization pulse shaping with the tomographic reconstruction of photoelectron wave packets. The physical scheme is based on the interference of a probe wave packet from $N+1$ resonance-enhanced multiphoton ionization via the target states and a reference wave packet from $M+1$ multiphoton ionization of the ground state. To create the wave packets, we employ carrier-envelope phase stable bichromatic ($M\omega$:$N\omega$) pump-probe pulse sequences. The scheme is demonstrated on femtosecond Rydberg wave-packet dynamics in potassium atoms using corotating circularly polarized (2ω:3ω) pulse sequences. The interference of continuum states with different angular momenta yields a crescent-shaped photoelectron wave packet rotating in the laser polarization plane due to the interplay of the optical phase and the accumulated quantum phase. Carrier-envelope phase control of the rotation provides access to the photoelectron asymmetry, enabling background-free detection of the crescent's angular motion which maps the bound-electron dynamics.

DOI: 10.1103/PhysRevA.101.013430

I. INTRODUCTION

The phase-sensitive detection of ultrafast dynamics has recently attracted much attention [1–5]. Different interferometric [3,6–11] and holographic [11–15] techniques have been devised to that end. The fundamentals of holographic imaging have been developed in optics by Gábor [16], honored by the Nobel Prize in 1971 [17], and were later extended to ultrafast optics [18,19]. The general scheme of holography is based on the interference of an object (also termed signal or probe) wave and a reference wave. The object path involves the target to be measured, whereas the reference path bypasses the target. After recombination of both paths, the target can be reconstructed from the interference pattern, provided the reference wave is well characterized. The application of this concept to the measurement of electronic wave functions in terms of both amplitude and phase was initially proposed by Leichtle *et al.* [1]. Since then, various experimental implementations of quantum state holography have been reported [20–23].

Here we present a technique for holographic imaging of ultrafast quantum dynamics. The technique is based on the creation of sculpted free-electron wave packets by interference of different multiphoton ionization (MPI) paths [24–27] using shaper-generated bichromatic femtosecond laser pulse sequences [28,29]. Recently, we have applied the method to create and control photoelectron wave packets with unusual symmetry properties, employing phase-stable polarization-tailored bichromatic pulses with commensurable frequencies [26,27]. In particular, we demonstrated the creation of a crescent-shaped photoelectron wave packet by nonresonant MPI of sodium atoms using (3ω:4ω) corotating circularly polarized (COCP) pulses [27]. It was shown that the orientation of the crescent in the laser polarization plane is controlled by the optical phases, in particular, the carrier-envelope phase (CEP). In a resonantly enhanced MPI (REMPI) scenario, however, the rotation is additionally sensitive to quantum phases, introduced either by the excitation itself, for example, due to Stark shifts, or during the subsequent time evolution of the system. Hence, for fixed optical phases, the highly asymmetric crescent acts like a pointer indicating the accumulated quantum phase by its rotation angle, reminiscent of the hands of a clock [30].

In this work we utilize the photoelectron crescent as a spectroscopic tool to obtain holographic information on ultrafast bound-electron dynamics. In contrast to our previous study, where the crescent rotation was manipulated via the optical phases [27], here we analyze the angular dynamics of the crescent induced by the time evolution of electronic wave packets propagating in the excited quantum system. The general scheme is based on the use of time-delayed bichromatic COCP pulse sequences with one color serving as a pump and the other color serving simultaneously as a probe and a reference pulse [31,32]. The pump pulse initiates the bound target wave packet via N-photon excitation. The probe pulse ionizes the system from the excited target states and maps the bound dynamics into a probe photoelectron wave packet. Effectively, the probe wave packet results from a time-delayed bichromatic $N+1$ REMPI process. The twist of the holographic technique is that the probe pulse simultaneously creates a reference photoelectron wave packet by direct single-color $M+1$ MPI from the ground state ($M \neq N$). Energetic overlap of the probe and reference wave packet in the continuum requires $N\omega_{pu} + \omega_{pr} = (M+1)\omega_{pr}$. This relation is fulfilled by choosing commensurable central frequencies of the pump and probe pulse with $N\omega_{pu} = M\omega_{pr}$ (spectral overlap in the bound system), i.e., by employing bichromatic ($M\omega$:$N\omega$) pump-probe pulse sequences (see Fig. 1). Due to the different numbers of photons absorbed on each ionization path, the resulting interference pattern of the probe and the reference wave packet in the continuum is sensitive to the CEP [26,27].

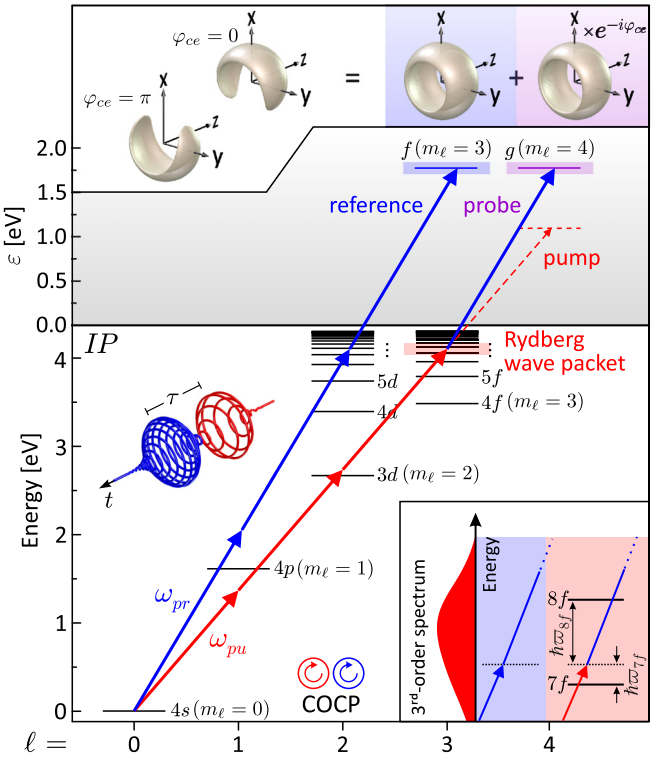

FIG. 1. Holographic excitation scheme of K atoms interacting perturbatively with a COCP (2ω:3ω) pump-probe pulse sequence. The red pulse (pump) launches an nf-type Rydberg wave packet by three-photon excitation. The time-delayed blue pulse acts as both a probe and a reference pulse, mapping the Rydberg dynamics into a g-type photoelectron wave packet and simultaneously creating an f-type reference wave packet (top inset). The interference of both partial waves gives rise to a crescent-shaped total wave packet. The orientation of the crescent is controlled by the optical phase, in particular the CEP, and the accumulated quantum phase, encoding holographic information on the bound-state-electron dynamics. The bottom inset shows a close-up of the primarily excited Rydberg states $7f$ and $8f$ lying within the bandwidth of the third-order pump spectrum.

In the COCP case, the CEP dependence induces a rotation of the photoelectron asymmetry in the polarization plane. The use of energy- and angle-resolved photoelectron detection enables us to utilize this controlled rotation to separate the symmetric and the antisymmetric part of the photoelectron density. Both parts deliver complementary spectroscopic information. Their joint analysis allows for the independent and unambiguous characterization of individual quantum states in the bound-electron wave packet. Direct experimental access to the antisymmetric part, moreover, provides background-free observation of the crescent dynamics, thus enhancing the contrast of the holographic technique. In combination, the CEP-sensitive interference of photoelectron wave packets with different angular momenta and the use of differential detection techniques for their measurement are the key to the holographic observation of ultrafast dynamics imprinted in the photoelectron asymmetry.

The paper is structured as follows. We start in Sec. II with a description of the physical system, including the theoretical background of our holographic technique and the experimental setup and strategy. The experimental results are presented in Sec. III. In Sec. III A we focus on the symmetric part of the measured time-resolved photoelectron spectra, which yields spectroscopic information on the beatings between pairs of excited bound states. In Sec. III B we evaluate the antisymmetric part of those spectra describing the beating between the individual states and the probe pulse. We present tomographic reconstructions of the three-dimensional (3D) photoelectron density for selected time delays to demonstrate its crescent shape and illustrate its angular dynamics. We summarize in Sec. IV.

II. PHYSICAL SYSTEM

In this section we introduce the physical system and describe our experiment. To motivate the experimental strategy for the holographic reconstruction of ultrafast electron dynamics, we start with a theoretical description of the probe and the reference wave packet, both of which are created by the probe pulse after resonant multiphoton excitation of the Rydberg dynamics by the pump.

A. Theoretical background

The dynamic quantum state holography technique introduced in Sec. I is demonstrated on Rydberg wave-packet dynamics in potassium atoms serving as a prototype for ultrafast electron dynamics. The excitation scheme for K atoms interacting perturbatively with a COCP (2ω:3ω) pulse sequence is depicted in Fig. 1. An nf-type Rydberg wave packet is created via three-photon excitation ($N=3$) by a red pump pulse $\tilde{E}^{+}_{pu}(\omega)$ centered at $\omega_{pu}=2.06$ rad/fs ($\lambda_{pu}=915$ nm). The blue probe pulse $\tilde{E}^{+}_{pr}(\omega)$, centered at $\omega_{pr}=3.09$ rad/fs ($\lambda_{pr}=610$ nm), maps the dynamics into a g-type continuum. Simultaneously, the blue pulse acts as a reference pulse providing an f-type reference wave packet by direct $2+1$ REMPI from the ground state ($M=2$). Due to the commensurable central frequencies, with $3\omega_{pu}=2\omega_{pr}$, the probe and the reference wave packet interfere at $3\hbar\omega_{pu}+\hbar\omega_{pr}=3\hbar\omega_{pr}$ in the continuum, enabling holographic measurement of the Rydberg dynamics similar to the quantum state holography reported in [1,20,33]. Despite its polarization, the electric field of the pulse sequence is completely described by a scalar function, i.e., by the circular field component. In frequency domain, we express the field by its positive-frequency spectrum

$$\begin{aligned}\tilde{E}^{+}(\omega) &= \tilde{E}^{+}_{pu}(\omega)+\tilde{E}^{+}_{pr}(\omega)\\ &= \tilde{\mathcal{E}}_{pu}(\omega-\omega_{pu})e^{i[\varphi_{ce}-\varphi_{pu}(\omega)]}\\ &\quad+\tilde{\mathcal{E}}_{pr}(\omega-\omega_{pr})e^{i[\varphi_{ce}-\varphi_{pr}(\omega)]},\end{aligned}\tag{1}$$

where $\tilde{\mathcal{E}}_{\nu}(\omega)$ ($\nu=pu,pr$) are the spectral envelopes of the two colors, ω_{ν} are the corresponding central frequencies, φ_{ce} is the common CEP, and $\varphi_{\nu}(\omega)$ are spectral phase modulation functions [28,34,35]. In the pump-probe experiment presented here, the pump pulse is advanced in time by application of a linear spectral phase $\varphi_{pu}(\omega)=\tau(\omega-\omega_{pu})$, with $\tau<0$. To avoid the additional τ-dependent optical phase introduced by a mechanical interferometer, we applied the linear phase with

respect to the central frequency ω_{pu}. By this means, only the temporal envelope of the pump is shifted while the carrier oscillation remains fixed [36]. For optimal time resolution, the probe pulse was chosen to be bandwidth limited, i.e., $\varphi_{pr}(\omega) \equiv 0$. Residual spectral phases introduced by optical elements in the beamline were compensated by adding the inverse of these phases to $\varphi_{pu}(\omega)$ and $\varphi_{pr}(\omega)$ [28]. The corresponding electric field in time domain is obtained by the inverse Fourier transformation $\mathcal{F}^{-1}$ of Eq. (1) as

$$\begin{aligned} E^+(t;\tau) &= E^+_{pu}(t;\tau) + E^+_{pr}(t) \\ &= \mathcal{E}_{pu}(t-\tau)e^{i(\omega_{pu}t+\varphi_{ce})} + \mathcal{E}_{pr}(t)e^{i(\omega_{pr}t+\varphi_{ce})}. \end{aligned} \tag{2}$$

The temporal pulse envelopes $\mathcal{E}_\nu(t) = \mathcal{F}^{-1}[\tilde{\mathcal{E}}_\nu](t)$ are the inverse Fourier transforms of the spectral amplitudes $\tilde{\mathcal{E}}_\nu(\omega)$. Assuming a left-handed circularly polarized pump pulse, the dipole selection rules for σ^+ transitions starting from the s-type ground states read $\Delta\ell = \Delta m = +1$. Therefore, three-photon excitation by the pump populates only Rydberg states with $\ell = 3$ and $m_\ell = 3$. In the absence of intermediate resonances, this nf-type Rydberg wave packet is composed of those states $|n\ell, m_\ell\rangle = |nf, 3\rangle$ $(n_{\min} \leqslant n \leqslant n_{\max})$ within the bandwidth of the third-order pump spectrum $\tilde{E}^{(3)}_{pu}(\omega) = \mathcal{F}[(E^+_{pu})^3](\omega)$ (see the bottom inset in Fig. 1). For a quasi-one-electron system, such as the K atom, the Rydberg wave packet can be written in spherical coordinates $\boldsymbol{r} = (r, \theta, \phi)$ as

$$\psi(\boldsymbol{r}, t; \tau) = \sum_{n=n_{\min}}^{n_{\max}} f_n(t;\tau) R_{n,3}(r) Y_{3,3}(\theta,\phi) e^{-i\omega_n t}, \tag{3}$$

with $f_n(t,\tau)$ the population amplitudes and ω_n the eigenfrequencies of the excited Rydberg states. The functions $R_{n,3}(r)$ and the spherical harmonic $Y_{3,3}(\theta,\phi)$ describe the corresponding radial and angular parts, respectively. The population amplitudes depend parametrically on τ through the time delay of the pump pulse relative to the probe. In the weak-field limit, these amplitudes are calculated using third-order time-dependent perturbation theory [37–40]. Using the negative-frequency analytic signal of the laser electric field and applying the rotating-wave approximation, the amplitudes read

$$\begin{aligned} f_n(t;\tau) &= \frac{\mu^{(3)}_{ns}}{(i\hbar)^3} \int_{-\infty}^{t} \mathcal{E}^3_{pu}(t'-\tau) e^{-i[(3\omega_{pu}-\omega_n)t'+3\varphi_{ce}]} dt' \\ &\xrightarrow{t\to\infty} \frac{\mu^{(3)}_{ns}}{(i\hbar)^3} \tilde{\mathcal{E}}^{(3)}_{pu}(3\omega_{pu}-\omega_n) e^{-i(3\omega_{pu}-\omega_n)\tau} e^{-i3\varphi_{ce}}. \end{aligned} \tag{4}$$

Herein $\mu^{(3)}_{ns}$ is the effective three-photon dipole coupling element between the s-type ground state and the Rydberg state nf, including the radial and angular coupling of all intermediate states, and $\tilde{\mathcal{E}}^{(3)}_{pu}(\omega)$ denotes the third-order spectrum of the envelope $\mathcal{E}_{pu}(t)$. In the second step we made use of the Fourier shift theorem. After the excitation, i.e., for times longer than the pump pulse duration Δt, the population amplitudes become time independent. Their modulus squared is determined by the power spectral density of the third-order pump spectrum evaluated at the three-photon transition frequency. The Rydberg wave packet in Eq. (3) then undergoes the free time evolution determined by the eigenfrequencies ω_n.

Next we consider the free-electron wave packet created by the probe pulse $E^+_{pr}(t)$. The left-handed circularly polarized probe maps the Rydberg dynamics via one-photon ionization into a g-type continuum with $m_\ell = 4$ and simultaneously creates an f-type reference wave packet with $m_\ell = 3$ by $2+1$ REMPI from the ground state. By design of the commensurable central frequencies, fulfilling $3\omega_{pu} + \omega_{pr} = 3\omega_{pr}$, both wave packets are created in the same energy window, allowing them to interfere. Their interference, as will be shown below [cf. Eq. (8)], is CEP sensitive, since the two ionization paths comprise different numbers of photons [26,27,41,42]. The total photoelectron wave packet is a superposition of the probe and the reference wave packet. In momentum representation, with the photoelectron momentum $\boldsymbol{k} = (k, \theta, \phi)$, we write

$$\begin{aligned} \tilde{\psi}(\boldsymbol{k};\tau) &= \tilde{\psi}_{pr}(\boldsymbol{k};\tau) + \tilde{\psi}_{\mathrm{ref}}(\boldsymbol{k}) \\ &= a_{pr}(k;\tau) Y_{4,4}(\theta,\phi) + a_{\mathrm{ref}}(k) Y_{3,3}(\theta,\phi). \end{aligned} \tag{5}$$

The population amplitudes $a_{pr}(k;\tau)$ and $a_{\mathrm{ref}}(k)$ of the continuum states are calculated in analogy to Eq. (4) by employing first- and third-order perturbation theory, respectively [43,44]. For the amplitudes of the probe wave packet, after the excitation by the pump pulse, we obtain

$$\begin{aligned} a_{pr}(k;\tau) &= \sum_n \frac{\mu_{kn}}{i\hbar} f^\infty_n(\tau) \\ &\quad \times \int_{-\infty}^{\infty} \mathcal{E}_{pr}(t) e^{-i[(\omega_{pr}+\omega_n-\omega_{ip}-\omega_k)t+\varphi_{ce}]} dt \\ &= \sum_n c^g_n(k) e^{-i(3\omega_{pu}-\omega_n)\tau} e^{-i4\varphi_{ce}}, \end{aligned} \tag{6}$$

with $f^\infty_n(\tau) = f_n(\infty;\tau)$, the ionization potential $\hbar\omega_{ip}$, and $\hbar\omega_k = \frac{\hbar^2 k^2}{2m_e}$ the kinetic energy of the photoelectron. The coefficients $c^g_n(k)$ are introduced as abbreviations describing the k dependence of the amplitudes. For the reference wave packet we find

$$\begin{aligned} a_{\mathrm{ref}}(k) &= \frac{\mu^{(3)}_{ks}}{(i\hbar)^3} \int_{-\infty}^{\infty} \mathcal{E}^3_{pr}(t) e^{-i[(3\omega_{pr}-\omega_{ip}-\omega_k)t+3\varphi_{ce}]} dt \\ &= c^f(k) e^{-i3\varphi_{ce}}. \end{aligned} \tag{7}$$

While the reference wave packet exhibits a phase of $3\varphi_{ce}$, the probe wave packet in Eq. (6) displays a phase of $4\varphi_{ce}$. This difference in the CEP sensitivity of both partial waves is the basis for the differential data analysis described in Sec. II B, which provides background-free access to the photoelectron asymmetry encoding holographic information of the Rydberg dynamics. Inserting these expressions into Eq. (5) and

calculating the modulus square of the wave function, the total photoelectron density $\varrho(\boldsymbol{k};\tau) = |\tilde{\psi}(\boldsymbol{k};\tau)|^2$ measured in the experiment is described by (arguments are omitted for ease of notation)

$$\varrho(\boldsymbol{k};\tau) = |\tilde{\psi}_{pr}(\boldsymbol{k};\tau) + \tilde{\psi}_{\mathrm{ref}}(\boldsymbol{k})|^2 = |c^f Y_{3,3}|^2 + \sum_n \left|c_n^g Y_{4,4}\right|^2 + 2\,\mathrm{Re}\left\{\sum_{\substack{n,\,m\\ n>m}} c_n^g \left(c_m^g\right)^* |Y_{4,4}|^2 e^{i\omega_{nm}\tau} + \sum_n c_n^g (c^f)^* |Y_{3,3}^* Y_{4,4}| e^{i\phi} e^{i\varpi_n \tau} e^{-i\varphi_{ce}}\right\}. \tag{8}$$

Here $\omega_{nm} = \omega_n - \omega_m$ are the transition frequencies between pairs of excited Rydberg states and $\varpi_n = \omega_n - 3\omega_{pu}$ are the three-photon detunings between the individual Rydberg states and the pump pulse (see Fig. 1). Since $3\omega_{pu} = 2\omega_{pr}$, the latter may also be conceived as beating frequencies of the Rydberg states and the second harmonic of the probe. The first term in Eq. (8), proportional to $|Y_{3,3}|^2$, is the density of the reference wave packet. This contribution describes a static, i.e., τ-independent, f-type torus-shaped background signal. The second and third terms, proportional to $|Y_{4,4}|^2$, are the density of the probe wave packet including a τ-dependent quantum phase. This g-type contribution is also torus shaped and describes the beating between any two excited Rydberg states nf and mf at the frequencies ω_{nm}, which we refer to as Rydberg beating modes. This contribution provides spectroscopic information on the Rydberg dynamics similar to [32]. Together, the first three terms constitute a dynamical but angularly symmetric signal. The last term in Eq. (8) is a mixing term resulting from the interference of probe and reference wave packet. This contribution contains holographic information on the Rydberg dynamics and is exploited for quantum phase retrieval. It maps the beating between the Rydberg states and the second harmonic of the probe at the frequencies ϖ_n in the continuum. Due to the different angular momenta of the probe and reference wave packet, the interference term is proportional to the product $|Y_{3,3}^* Y_{4,4}|$ and therefore retains an azimuthal phase factor of $e^{-i\phi}$. The corresponding angular distribution is antisymmetric and has the shape of a bipolar crescent, i.e., a positive and a negative crescent facing one another [see the insets in Fig. 2(b)] [27,45]. The rotation angle of the crescent in the laser polarization plane indicates the ionization phase $\beta_n = \arg[c_n^g (c^f)^*]$ and the accumulated quantum phase $\varpi_n \tau$. In addition, the rotation is controlled by the CEP [27]. As illustrated in the top inset in Fig. 1, a variation of the CEP by $\Delta\varphi_{ce} = \pi$ inverts the photoelectron asymmetry. In the present paper we utilize this CEP dependence to separate the antisymmetric crescent-shaped signal from the symmetric torus-shaped signal. By measuring the photoelectron momentum distribution (PMD) for $\varphi_{ce} = 0$ and $\varphi_{ce} = \pi$ and subtracting the results, we eliminate the CEP-independent symmetric signal. The resulting density difference

$$\Delta\varrho^-(\boldsymbol{k};\tau) = \frac{\varrho(\boldsymbol{k};\tau,\varphi_{ce}=0) - \varrho(\boldsymbol{k};\tau,\varphi_{ce}=\pi)}{2} = \sum_n C_n(\boldsymbol{k}) \cos(\phi + \varpi_n \tau + \beta_n), \tag{9}$$

with $C_n = 2|c_n^g (c^f)^* Y_{3,3}^* Y_{4,4}|$, extracts the antisymmetric part of the total density $\varrho(\boldsymbol{k};\tau)$. Provided the probe frequency ω_{pr} is known, Fourier analysis of this part with respect to the time delay τ delivers the absolute frequencies ω_n of the involved Rydberg states through the detunings ϖ_n. By adding both results, we obtain the symmetric part of the density

$$\Delta\varrho^+(\boldsymbol{k};\tau) = \frac{\varrho(\boldsymbol{k};\tau,\varphi_{ce}=0) + \varrho(\boldsymbol{k};\tau,\varphi_{ce}=\pi)}{2} = A(\boldsymbol{k}) + \sum_{\substack{n,\,m\\ n>m}} B_{nm}(\boldsymbol{k}) \cos(\omega_{nm}\tau + \alpha_{nm}), \tag{10}$$

with the static background $A = |c^f Y_{3,3}|^2 + \sum_n |c_n^g Y_{4,4}|^2$, the beating amplitudes $B_{nm} = 2|c_n^g (c_m^g)^*||Y_{4,4}|^2$, and the ionization phases $\alpha_{nm} = \arg[c_n^g (c_m^g)^*]$. This part gives us spectroscopic information on the Rydberg beating modes as described, for example, in [7,32,46–48]. The relations $\omega_{nm} = \varpi_n - \varpi_m$ and $\alpha_{nm} = \beta_n - \beta_m$ provide the link between the symmetric and the antisymmetric part, which we will make use of in the data evaluation presented in Sec. III B. The joint information of both parts allows us to independently determine the eigenenergy of each excited Rydberg state.

To illustrate the dynamics of the two density differences $\Delta\varrho^\pm(\boldsymbol{k};\tau)$, both are shown in Fig. 2 for a generic Rydberg model. The model includes the two Rydberg states $7f$ and $8f$, which are also excited in the experiment (see Sec. III A), with the same population. The time evolution of both states is mapped onto the continuum by a Gaussian-shaped probe pulse with the same central frequency as in the experiment. To establish a close connection to the 2D projections detected in the experiment, we introduce the Abel transform [49,50] of $\Delta\varrho^\pm(\boldsymbol{k};\tau)$ in the x direction

$$\Delta\varrho^\pm_{\mathrm{proj}}(p,\theta;\tau) = \int_{-\infty}^{\infty} \Delta\varrho^\pm(\boldsymbol{k};\tau)\, dk_x, \tag{11}$$

where p denotes the transverse photoelectron momentum in the y-z plane. Furthermore, we introduce the total photoelectron yield emitted into the right hemisphere

$$\Delta\varrho^\pm_{\mathrm{int}}(\tau) = \int_0^\infty \int_0^\pi \Delta\varrho^\pm_{\mathrm{proj}}(p,\theta;\tau)\, d\theta\, dp \tag{12}$$

to obtain a scalar quantity sensitive to both the photoelectron yield and asymmetry. Both yield curves are plotted in Fig. 2

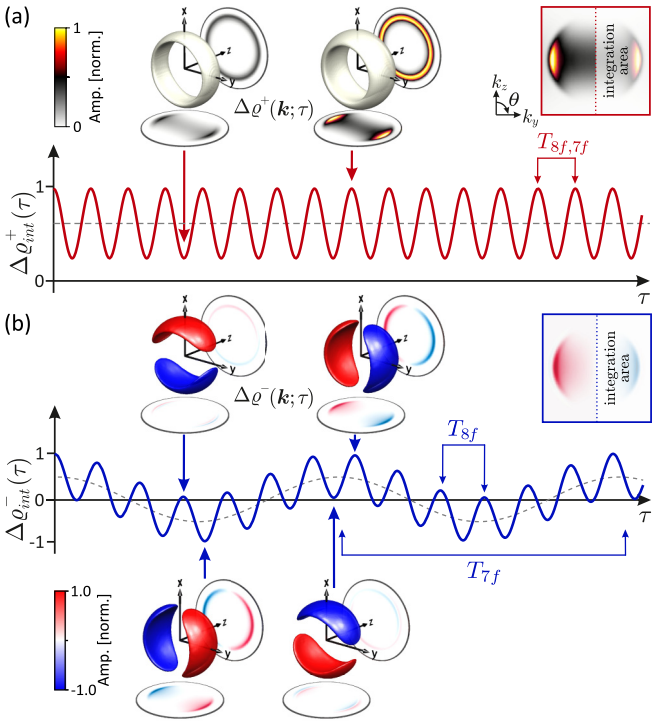

FIG. 2. Illustration of the symmetric and antisymmetric part of the photoelectron wave packet for a generic Rydberg model comprising the Rydberg states $7f$ and $8f$. (a) Dynamics of the symmetric difference density $\Delta\varrho^{+}(\boldsymbol{k};\tau)$, integrated over the right hemisphere, shown as the red curve. Three-dimensional representations are shown for two selected time delays τ of minimum and maximum yield, respectively. (b) Integrated difference density $\Delta\varrho^{-}(\boldsymbol{k};\tau)$ as a function of τ (blue curve). The 3D representations illustrate the bipolar crescent rotating in the laser polarization plane due to the accumulated quantum phase. The surface color encodes the sign of the antisymmetric angular distribution.

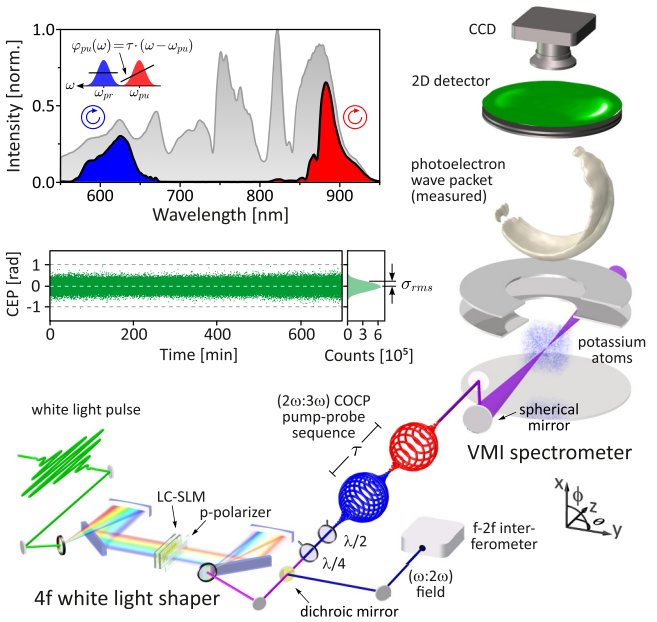

FIG. 3. Experimental setup. Time-delayed COCP (2ω:3ω) pulse sequences are generated by bichromatic amplitude and phase modulation of a WLS using a $4f$ polarization shaper and a $\lambda/4$ plate. The top inset shows a measured bichromatic amplitude profile together with the input WLS (gray-shaded background). Long-term CEP stability with rms fluctuations of $\sigma_{\mathrm{rms}} = 215$ mrad/fs (middle inset) is achieved by picking an additional (ω:2ω) field from the edges of the WLS to feed an f-$2f$ interferometer coupled to the control loop of the laser system. Photoelectron wave packets created by the interaction of K atoms with the bichromatic pump-probe sequence are imaged by a VMI spectrometer. Projections of the crescent-shaped wave packets are measured by a position-sensitive 2D detector and recorded by a CCD camera. For the tomographic reconstruction of the wave packets, a $\lambda/2$ plate is used to rotate the pulses about the z axis.

as a function of τ. For selected time delays, the corresponding 3D density differences $\Delta\varrho^{\pm}(\boldsymbol{k};\tau)$ are shown, along with the 2D projections $\Delta\varrho^{\pm}_{\mathrm{proj}}(\boldsymbol{k};\tau)$ in the x direction (detector plane) and in the z direction (polarization plane). The yield $\Delta\varrho^{+}_{\mathrm{int}}(\tau)$ of the symmetric part, depicted in Fig. 2(a), exhibits a pronounced oscillation at the beating frequency $\omega_{8f,7f}$, centered around a constant offset (gray dashed line). The two selected 3D graphs display symmetric torus-shaped angular distributions with different peak amplitudes. The distributions result from the interference of two g-type wave packets probing the Rydberg states. The amplitude modulation is due to the beating of the two tori at $\omega_{8f,7f}$.

The yield $\Delta\varrho^{-}_{\mathrm{int}}(\tau)$ of the antisymmetric part is depicted in Fig. 2(b). It describes a superposition of two oscillations reflecting the coherent motion of two bipolar crescents created by the interference of the g-type probe wave packets and the f-type reference wave packet. In the model scenario, both contributions are counterrotating in the polarization plane with the angular velocities $\varpi_{7f} = -13$ mrad/fs and $\varpi_{8f} = 86$ mrad/fs, respectively (see also Sec. III B). The former gives rise to the slow amplitude modulation with a period of $T_{7f} = 2\pi/\varpi_{7f} = 480$ fs, while the latter is responsible for the fast oscillation with a time constant of $T_{8f} = 2\pi/\varpi_{8f} = 73$ fs (see the bottom inset in Fig. 1). The coherent sum of two bipolar crescents is again a bipolar crescent with modulated peak amplitude and orientation. This effective bipolar distribution is shown in the selected 3D graphs. All four graphs are normalized to highlight the rotational dynamics of the antisymmetric density difference. The amplitude modulation due to the beating of the two counterrotating crescents is discernible in the backward (z) projections. The combination of both effects determines the yield variation of the photoelectrons in the right hemisphere. This example highlights that differential, i.e., angle-resolved, measurement is indispensable for the observation of the antisymmetric contribution which vanishes upon full angular integration.

B. Experimental setup and strategy

In our experiment, we combine bichromatic white light polarization pulse shaping [29] with photoelectron imaging [51] and tomography techniques [52]. A schematic overview of the experimental setup is depicted in Fig. 3. Infrared input pulses provided by an actively CEP-stabilized multipass chirped pulse amplifier (FEMTOLASERS Rainbow 500, CEP4 module, Femtopower HR 3 kHz, with $\lambda_0 = 790$ nm and 1.0 mJ

pulse energy) are used to seed a neon-filled hollow-core fiber (absolute gas pressure of 2.5 bars) for the generation of an octave-spanning white light supercontinuum (WLS). The white light pulses are modulated in frequency domain using a home-built $4f$ polarization pulse shaper [28,34,35] specifically adapted to the ultrabroadband WLS [29]. Bichromatic amplitude and phase modulation is implemented by a dual-layer liquid-crystal spatial light modulator (Jenoptik SLM-640d) and a broadband p polarizer (CODIXX colorPol) mounted in the Fourier plane of the $4f$ setup. In this configuration, the shaper provides horizontally polarized bichromatic fields. For the conversion from linear to corotating circular polarization, we use a superachromatic $\lambda/4$ waveplate (Bernhard Halle Nachfl.) at the shaper output. A measured sample spectrum of the (2ω:3ω) COCP fields employed in the experiment is shown in the top inset in Fig. 3. The spectral bandwidth of the pump pulse is $\Delta\omega_{pu} = 0.09$ rad/fs (red band), corresponding to a bandwidth-limited pulse duration of $\Delta t_{pu} \approx 22$ fs. The pump bandwidth is chosen sufficiently narrow to address only a few Rydberg states within the nf series. This allows for a transparent analysis of the experimental results, in particular, the dynamics of the photoelectron crescent (see Sec. III B). The bandwidth of the probe pulse $\Delta\omega_{pr} = 0.14$ rad/fs (blue band), corresponding to a bandwidth-limited pulse duration of $\Delta t_{pr} \approx 12$ fs, was chosen somewhat larger to increase the time resolution of the probe step. Using the central wavelengths $\lambda_{pu} = 915$ nm and $\lambda_{pr} = 610$ nm (cf. Sec. II A), the energetic overlap of the probe and the reference wave packet in the continuum occurs around the kinetic energy $\varepsilon = 3\hbar\omega_{pu} + \hbar\omega_{pr} - \hbar\omega_{ip} \approx 1.77$ eV (see Fig. 1). The peak amplitudes of the two colors were chosen in a two-step procedure. First we adjusted the amplitudes coarsely by matching the yield of the one-color photoelectron signals produced by each color alone. Second we applied a CEP sweep (-6π to 6π) via the CEP stabilization unit of the laser system and used the shaper to fine-tune the amplitudes by maximizing the asymmetry contrast of the two-color signal inspected online on the detector. For the time-resolved studies, a linear spectral phase $\varphi_{pu}(\omega) = \tau(\omega - \omega_{pu})$ is applied to the red band to advance the pump pulse in time by a variable time delay τ (see the top inset in Fig. 3). By applying the linear spectral phase relative to ω_{pu} (as opposed to $\omega = 0$), the envelope of the pump is shifted while its carrier remains fixed. Therefore, no additional τ-dependent optical phase is introduced by the time delay, in contrast to an interferometric setup. Owing to the common-path geometry of the shaper-based scheme, the generated bichromatic pulse sequences are inherently phase locked [53]. To achieve the CEP stability required for the holographic pump-probe studies presented in Sec III B, we use an external active CEP-stabilization loop. An additional (ω:2ω) field is extracted from the spectral edges of the WLS by the shaper, split off the main beam by a dichroic mirror and sent to a single-shot f-$2f$ interferometer feeding the control loop of the laser system [26]. The central inset to Fig. 3 shows a long-term monitoring of the CEP (green dots) recorded by the f-$2f$ interferometer during the tomographic measurements presented in Sec. III B [see Fig. 7(a)]. Over a period of 11 h, the CEP fluctuations are measured to be $\sigma_{\mathrm{rms}} = 215$ mrad root mean square (rms).

The bichromatic pulse sequences are focused via a spherical mirror ($f = 250$ mm) into the interaction region of a velocity map imaging (VMI) spectrometer [51] filled with K vapor from a dispenser source (SAES Getters). The target pressure is 5×10^{-7} mbar, at a background pressure of 2×10^{-7} mbar. The total pulse energy measured at $\tau = 0$ is $E_{\mathrm{tot}} = 1.17$ μJ. From the pulse spectrum in Fig. 3 (top inset), we derive an energy distribution among the two colors of $E_{pu} = 0.61$ μJ and $E_{pr} = 0.56$ μJ. With a measured focal beam waist of $w_0 = 30$ μm and the bichromatic pulse parameters given above, we estimate the individual peak intensities $I_{0,pu} \approx 2 \times 10^{12}$ W/cm^2 and $I_{0,pr} \approx 3 \times 10^{12}$ W/cm^2. The photoelectron wave packets created by atomic MPI are projected onto a position-sensitive 2D detector (Scientific Instruments S3075-10-I60-PS43-FM) consisting of a dual-layer microchannel plate in chevron configuration stacked with a phosphor screen. The 2D images are recorded by a charge coupled device (CCD) camera (Lumenera LW165M) using an exposure time of 150 ms. When the dispenser source is switched off, the total count rate reduces to 0.5%. Residual events are mainly attributed to detector dark counts, while the photoelectron contribution from the background gas is negligible. To retrieve the 3D PMD, we employ the Fourier-based tomographic technique introduced in [52]. Subsequently, photoelectron tomography is applied to the 3D imaging of PMDs from atomic strong-field ionization [54], the reconstruction of molecular PMDs in the laboratory [55] and the molecular [56] frame, and the retrieval of circularly polarized XUV fields from high-harmonic generation [57]. For the tomographic measurements, the input pulse sequence is rotated about the laser propagation direction using a superachromatic $\lambda/2$ waveplate. Each PMD is retrieved from 45 projections, measured with an angular step size of $\delta\phi = 4^\circ$, employing the Fourier slice algorithm [58].

In the experiment, we vary the time delay $\tau \in [-1000\ \mathrm{fs}, 50\ \mathrm{fs}]$ in steps of $\delta\tau = 5$ fs. For each step, we measure a pair of 2D projections $\mathcal{P}(p, \theta; \tau, \varphi_{ce})$ of the PMD, one for $\varphi_{ce} = 0$ and another one for $\varphi_{ce} = \pi$. A sample pair of measured spectra is depicted in Figs. 4(a) and 4(b). The spectra show the probe and/or reference signal centered at $\varepsilon = 1.77$ eV. In order to highlight this contribution, the one-color signal of the pump pulse, centered at $\varepsilon = 1.08$ eV (red dashed arrow in Fig. 1), and a signal attributed to bichromatic $2 + 1$ REMPI via the near-resonant $3d$ state, centered at $\varepsilon = 0.36$ eV, are filtered out numerically by applying a super-Gaussian high-pass filter to the spectra. The origin of the latter is identified by comparison with the numerical simulation. The spectra exhibit a pronounced lateral asymmetry in the y direction which is inverted by switching the CEP from 0 to π. By calculating the sum and the difference of each pair $\Delta\mathcal{P}^{\pm}(p, \theta; \tau) = \mathcal{P}(p, \theta; \tau, 0) \pm \mathcal{P}(p, \theta; \tau, \pi)$, we obtain the symmetric and the antisymmetric part of the spectra, respectively. This procedure is illustrated in Figs. 4(c) and 4(d). The resulting 2D images $\Delta\mathcal{P}^{\pm}(p, \theta; \tau)$ are almost perfectly symmetric or antisymmetric, except for tiny experimental imperfections. Because symmetrization and projection are commutative operations, the quantities $\Delta\mathcal{P}^{\pm}(p, \theta; \tau)$ derived from the measured data correspond to the projections of the density differences $\Delta\varrho^{\pm}(\boldsymbol{k}; \tau)$ introduced in Eqs. (9)

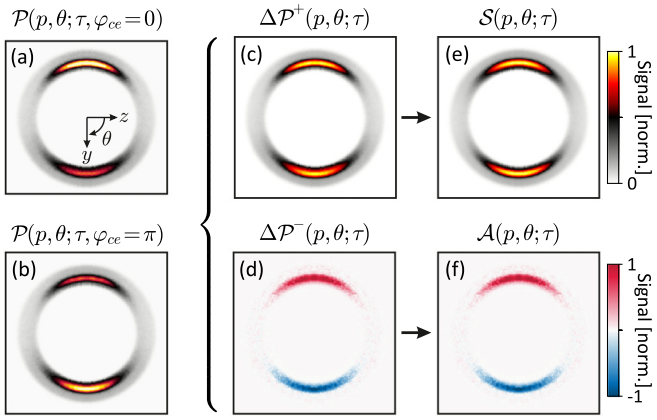

FIG. 4. Exemplification of the data evaluation procedure to extract the symmetric and antisymmetric parts of the PMD. The left column shows a pair of 2D projections $\mathcal{P}(p,\theta;\tau,\varphi_{ce})$ of the photoelectron density measured for (a) $\varphi_{ce}=0$ and (b) $\varphi_{ce}=\pi$. The middle column shows (c) the sum $\Delta\mathcal{P}^{+}(p,\theta;\tau)$ and (d) the difference $\Delta\mathcal{P}^{-}(p,\theta;\tau)$ of both spectra, revealing nearly symmetric and antisymmetric signals, respectively. In the right column the signals are almost indistinguishable from the corresponding (e) symmetric part $\mathcal{S}(p,\theta;\tau)$ and (f) antisymmetric part $\mathcal{A}(p,\theta;\tau)$.

and (10):

$$\Delta\mathcal{P}^{\pm}(p,\theta;\tau)\propto\Delta\varrho^{\pm}_{\mathrm{proj}}(p,\theta;\tau). \tag{13}$$

Therefore, the 2D images $\Delta\mathcal{P}^{\pm}(p,\theta;\tau)$ provide a direct link between the experimental data and the theoretical model described in Sec. II A. In order to eliminate minute experimental imperfections of the signals $\Delta\mathcal{P}^{\pm}(p,\theta;\tau)$, we calculate the respective symmetric part $\mathcal{S}(p,\theta;\tau)$ and antisymmetric part $\mathcal{A}(p,\theta;\tau)$ according to

$$\mathcal{S}(p,\theta;\tau)=\frac{\Delta\mathcal{P}^{+}(p,\theta;\tau)+\Delta\mathcal{P}^{+}(p,-\theta;\tau)}{2}, \tag{14}$$

$$\mathcal{A}(p,\theta;\tau)=\frac{\Delta\mathcal{P}^{-}(p,\theta;\tau)-\Delta\mathcal{P}^{-}(p,-\theta;\tau)}{2}. \tag{15}$$

These signals are evaluated and discussed in Sec. III. The symmetrized and antisymmetrized images of the example spectra are shown in Figs. 4(e) and 4(f). Only marginal differences from the images in Figs. 4(c) and 4(d) are discernible, confirming the high fidelity of the measurement. The signal $\mathcal{S}(p,\theta;\tau)$, associated with the symmetric part $\Delta\varrho^{+}(\boldsymbol{k},\tau)$ of the photoelectron density, reveals modulations of the integral photoionization cross section due to the Rydberg dynamics in the bound system. In contrast, the signal $\mathcal{A}(p,\theta;\tau)$, related to the antisymmetric part $\Delta\varrho^{-}(\boldsymbol{k},\tau)$ of the density, reveals variations of the differential cross section due to the angular dynamics of the photoelectron crescent. In the following section, both signals will be analyzed separately for wave-packet spectroscopy (Sec. III A) and wave-packet holography (Sec. III B). The dynamic quantum state holography technique presented here delivers both results in one measurement.

III. RESULTS AND DISCUSSION

In this section we present the experimental results and discuss our findings. We start in Sec. III A by evaluating

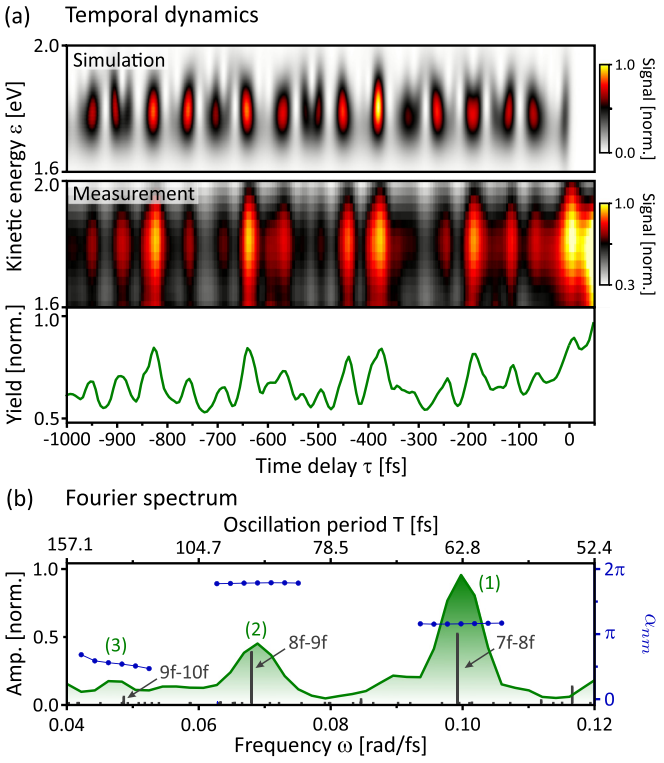

FIG. 5. Experimental results obtained by evaluation of the symmetric signal $\mathcal{S}(p,\theta;\tau)$. (a) Time-resolved photoelectron signal in the energy window of the probe or reference signal. The middle frame shows measured angle-integrated and energy-resolved photoelectron spectra. The results are compared to a numerical simulation shown in the top frame. The bottom frame shows the total photoelectron yield as a function of τ. (b) The Fourier spectrum of the τ-dependent yield (green line) reveals three prominent Rydberg beating modes attributed to the major excitation of the states $7f$ and $8f$ and minor excitation of states $9f$ and $10f$. The assignment of states is confirmed by a generic stick spectrum (gray lines) based on spectroscopic data from [59]. The blue dotted lines are the extracted ionization phases α_{nm}.

the symmetric part of the measured photoelectron spectra to retrieve spectroscopic information on the Rydberg beating modes. In Sec. III B we utilize the holographic properties of our method. By exploiting the CEP sensitivity of the interference between probe and reference wave packet we gain access to the antisymmetric part of the spectra providing independent information on the individual Rydberg states. In addition, we present tomographic reconstructions of the 3D PMD to demonstrate the crescent shape of the total photoelectron density and illustrate its angular dynamics.

A. Wave-packet spectroscopy

By analyzing the symmetric signal $\mathcal{S}(p,\theta;\tau)$ [cf. Eq. (14)] as a function of the time delay τ, we gain access to the beating of pairs of excited Rydberg states, similar to [32]. The experimental results are presented in Fig. 5. The middle frame of Fig. 5(a) shows time- and energy-resolved data, obtained by angular integration of $\mathcal{S}(p,\theta;\tau)$ over the interval $\theta\in[0^{\circ},180^{\circ}]$ (right detector hemisphere) in the relevant

TABLE I. Spectroscopic parameters derived from the experiment. (a) The symmetric part of the photoelectron density (cf. Sec. III A) provides information on the beating of pairs of excited Rydberg states nf, yielding the Rydberg beating modes ω_{nm} and the ionization phases α_{nm}. The corresponding oscillation periods $T_{nm} = 2\pi/\omega_{nm}$ are calculated from the measured beating modes. (b) The antisymmetric part of the density (cf. Sec. III B) delivers information on the beating between individual Rydberg states and the second harmonic of the probe pulse $2\omega_{pr}$, yielding the detunings ϖ_n (not listed) and the ionization phases β_n. In conjunction, both signals enable the independent characterization of the excited states in terms of eigenenergies $\hbar\omega_n$ and final populations (not listed). The reference data given in the last column are taken from the NIST database [59].

(a) Wave-packet spectroscopy

Mode	ω_{nm}[a] (mrad/fs)	T_{nm}[b] (fs)	α_{nm} (rad)	Beating	ω_{nm}[c] (mrad/fs)
(1)	99.4 ± 0.2	63.2 ± 0.1	4.15 ± 0.01	$7f - 8f$	99.195
(2)	68.3 ± 0.2	92.0 ± 0.3	5.94 ± 0.01	$8f - 9f$	67.984
(3)	46 ± 3	137 ± 9	1.8 ± 0.3	$9f - 10f$	48.617

(b) Wave-packet holography

Mode	$\hbar\omega_n$[a] (eV)	T_n[b] (fs)	β_n (rad)	Beating	$\hbar\omega_n$[c] (eV)
(i)	4.07 ± 0.01	491 ± 7.7	-0.99 ± 0.02	$7f - 2\omega_{pr}$	4.062317
(ii)	4.12 ± 0.01	73 ± 0.2	3.27 ± 0.01	$8f - 2\omega_{pr}$	4.127608

[a]Experimental results.
[b]Calculational results.
[c]Literature results.

energy window $\varepsilon \in [1.6\ \text{eV}, 2.0\ \text{eV}]$. Pronounced oscillations of the photoelectron yield are observed along the τ direction. The experimental data are compared to a simulation (top frame) based on the numerical solution of the time-dependent Schrödinger equation for the interaction of a hydrogenlike multilevel atom with a Gaussian-shaped bichromatic pump-probe pulse sequence compatible with the experimental parameters, but higher τ resolution [40]. Examination of the neutral population dynamics yields a final population of the f-type target states on the order of 1%, confirming the perturbative character of the excitation in the experiment. The energy-resolved photoelectron spectra are calculated using time-dependent perturbation theory (cf. Sec. II A). The temporal dynamics of the simulated signal is in good agreement with the experimental results. However, the simulation exhibits subtle dynamics in the ε direction which reflect the energetic structure of the Rydberg wave packet, because each Rydberg state nf is mapped into an individual energy window centered at $\varepsilon_n = \hbar\omega_n + \hbar\omega_{pr} - \hbar\omega_{ip}$. These windows are displaced by the eigenenergy difference of the corresponding Rydberg states, separating the time signals of the different beating modes energetically. In the experiment, these energetic signatures are not resolved.

The strong photoelectron signal measured around $\tau = 0$ but not reproduced in the simulation is due to bichromatic $2 + 2$ REMPI via the $4d$ state. When both pulses overlap in time, the $4d$ state is resonantly excited by frequency mixing of one red and one blue photon [25]. Ionization by another two red photons generates additional photoelectrons in the energy window of the probe or reference signal. In the simulation, we considered only one-photon ionization from the target states, which is relevant for $\tau > \Delta t_{pu}$. Therefore, these photoelectrons are absent in the simulation result.

Integration over the entire energy window delivers the total photoelectron yield emitted into the right hemisphere, analogously to the quantity $\Delta\varrho^{+}_{\text{int}}(\tau)$ described by Eq. (12). The integrated signal is plotted as a function of τ in the bottom frame. Fourier analysis of this signal, depicted as a green solid line in Fig. 5(b), reveals three distinct Rydberg beating modes at the frequencies $\omega_{(1)} = 99.4 \pm 0.2$ mrad/fs, $\omega_{(2)} = 68.3 \pm 0.2$ mrad/fs, and $\omega_{(3)} = 48 \pm 3$ mrad/fs. The errors are determined by fitting multiple Gaussians to the Fourier spectrum. These modes are identified as beatings between the Rydberg states (1) $7f$ and $8f$, (2) $8f$ and $9f$, and (3) $9f$ and $10f$ (see Table I). Their amplitudes indicate a major population of states $7f$ and $8f$, similar to the generic Rydberg model from Fig. 2, and only minor population of states $9f$ and $10f$. For comparison with spectroscopic data from the NIST database [59], a generic line spectrum including the Rydberg states $7f$–$23f$ is shown in gray. The corresponding amplitudes are determined by the third-order pump spectrum evaluated at the corresponding line frequencies (cf. Sec. II A). By considering a slight redshift of the pump spectrum, we achieve good qualitative agreement with the experimental spectrum. This effective redshift presumably is induced by the $3d$ state being nearly two-photon resonant with the pump pulse, as already discussed in [32]. From the Fourier analysis we also extract the ionization phases α_{nm}, i.e., the relative phases between the continuum amplitudes $c^g_n(k)$ and $c^g_m(k)$ [cf. Eq. (10)], which are shown as blue dotted lines in Fig. 5(b). These phases are almost flat for each individual mode with mean values of $\alpha_{8f,7f} = 4.15$ rad, $\alpha_{9f,8f} = 5.94$ rad, and $\alpha_{10f,9f} = 1.82$ rad. The above results will be used in the next section together with the information encoded in the antisymmetric signal to unambiguously characterize individual Rydberg states in the bound-state wave packet. A summary of the results derived from the symmetric signal is given in Table I(a).

B. Wave-packet holography

Next we analyze the temporal dynamics of the antisymmetric signal $\mathcal{A}(p, \theta; \tau)$ [cf. Eq. (15)]. This signal reflects the interference term arising from the coherent superposition

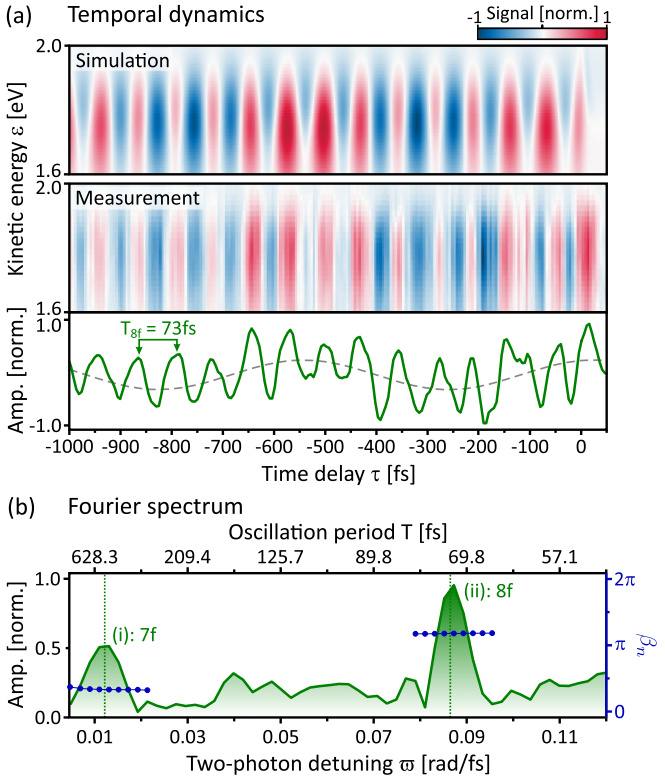

FIG. 6. Experimental results obtained by evaluation of the antisymmetric signal $\mathcal{A}(p,\theta;\tau)$. The figure is structured similarly to Fig. 5. (a) Time-resolved data, displaying a fast oscillation superimposed on a slow oscillation. The corresponding frequency components are revealed by the Fourier spectrum of the integrated time signal, shown in (b). The components are attributed to the beating of the primarily excited Rydberg states $7f$ and $8f$ with the second harmonic of the probe pulse and enable the independent spectroscopic characterizations of both Rydberg states. The extracted ionization phases β_n are shown as blue dotted lines.

of the probe and the reference wave packet [cf. Eq. (9)]. Therefore, $\mathcal{A}(p,\theta;\tau)$ carries the essential holographic information encoded in the rotation of the photoelectron crescent. The experimental results are presented in Fig. 6, in a similar manner as the results from the symmetric part in Fig. 5. The time signal shown in Fig. 6(a) alternates between positive and negative values depending on the orientation of the crescent in the polarization plane. Large positive values correspond to the crescent oriented preferentially in the $+y$ direction, while large negative values are indicative of the crescent oriented in the $-y$ direction. Zeros imply the crescent pointing upward or downward or, according to the discussion in Sec. II A, the vanishing of the complete difference density $\Delta\varrho^{-}(\boldsymbol{k};\tau)$. The high-resolution simulation shown in the top frame agrees well with the measured data in the middle frame.

The integrated signal shown in the bottom frame displays a superposition of two oscillations, similar to $\Delta\varrho^{-}_{\mathrm{int}}(\tau)$ in the generic Rydberg model shown in Fig. 2(b) [cf. Eq. (13)]. The gray dashed line serves as a guide to the eye, indicating the slow oscillation with a period of about $T = 480$ fs. The additional fast oscillation with a period of about $T = 73$ fs is clearly discernible. Figure 6(b) shows the Fourier analysis of the integrated signal. In this case, the frequency axis corresponds to the detuning ϖ between the second harmonic of the probe pulse $2\omega_{pr}$ and the eigenfrequencies ω_n of the Rydberg states [cf. Eq. (9)]. On the positive detuning axis, the Fourier spectrum exhibits two peaks centered at $|\varpi_{(i)}| = 12.8$ mrad/fs and $|\varpi_{(ii)}| = 86.4$ mrad/fs, indicating the excitation of essentially two Rydberg states. The corresponding periods are $T_{(i)} = 490.9$ fs and $T_{(ii)} = 72.7$ fs. However, since *a priori* the sign of the detunings is unknown, the Hermitian counterparts of these peaks on the negative detuning axis need to be considered as well. Altogether we hence find four possible detunings with $\varpi_{(i)} = \pm 12.8$ mrad/fs and $\varpi_{(ii)} = \pm 86.4$ mrad/fs. To unambiguously decide which pair of detunings corresponds to actual excited Rydberg states, we make use of the spectroscopic information derived from the symmetric signal $\mathcal{S}(p,\theta;\tau)$ in Sec. III A. By comparing all possible difference frequencies and relative ionization phases, we find that the negative $\varpi_{(i)}$ and positive $\varpi_{(ii)}$ components are consistent with the beating mode of the Rydberg states $7f$ and $8f$. The difference frequency

$$\begin{aligned}\varpi_{(ii)} - \varpi_{(i)} &= 86.4\ \text{mrad/fs} - (-12.8\ \text{mrad/fs}) \\ &= 99.2\ \text{mrad/fs} \end{aligned} \tag{16}$$

and relative ionization phase

$$\begin{aligned}\beta_{(ii)} - \beta_{(i)} &= 3.27\ \text{rad} - (-0.99\ \text{rad}) \\ &= 4.26\ \text{rad} \end{aligned} \tag{17}$$

are in excellent agreement with $\omega_{8f,7f}$ and $\alpha_{8f,7f}$ as listed in Table I(a). Therefore, we assign $\varpi_{7f} = \varpi_{(i)} = -12.8$ mrad/fs and $\varpi_{8f} = \varpi_{(ii)} = 86.4$ mrad/fs. With the second harmonic probe frequency $2\omega_{pr} = 6.18$ rad/fs, we retrieve the eigenenergies $\hbar\omega_{7f} = 4.07 \pm 0.01$ eV and $\hbar\omega_{8f} = 4.12 \pm 0.01$ eV, in good accordance with data reported in the literature [59]. In this case, the estimated errors are mainly determined by the uncertainty of the central frequencies of the two colors, due to their slightly asymmetric shapes (see the top inset in Fig. 3), for which we assume an error of 5 mrad/fs. The amplitudes of the two peaks suggest a two times more efficient population of the $8f$ state than the $7f$ state. All of these results are summarized in Table I(b).

The last part of the experiment is dedicated to the 3D mapping of the photoelectron crescent and its angular dynamics. To this end, we reconstructed the PMD tomographically for various characteristic time delays τ, keeping the CEP fixed at $\varphi_{ce} = 0$. Since the dynamics occurs on timescales of $T_{7f} = 480$ fs and $T_{8f} = 73$ fs, respectively, we sampled the time window $\tau \in [-750\ \text{fs}, -150\ \text{fs}]$ with a step size of $\delta\tau = 25$ fs. The experimental results are presented in Fig. 7(a). The middle frame displays the time series of angle-resolved (ϕ) and energy-integrated spectra as a function of τ. The experimental result (lower panel) is compared to a high-resolution simulation (upper panel) based on the same parameters as in Fig. 6(a). Reconstructed 3D PMDs with corresponding z projections are shown in the top and bottom row for selected time delays. The PMDs in the top row (green frames) were chosen to cover the period T_{8f}, illustrating the fast oscillation of the crescent, while the PMDs in the bottom row (orange frames) cover the period T_{7f} of the slow oscillation. Because the PMD reflects the total photoelectron density (being a

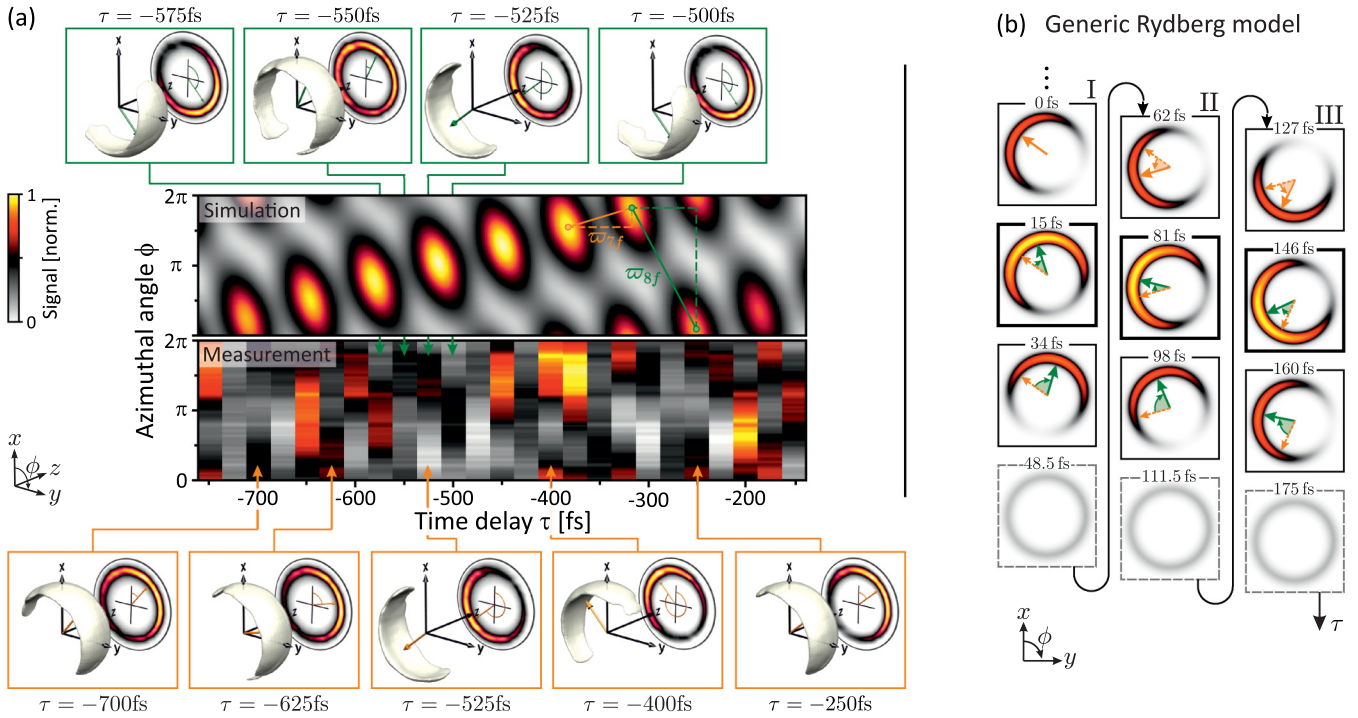

FIG. 7. Three-dimensional mapping of the photoelectron crescent and its dynamics. (a) Tomographic reconstruction of the photoelectron density for a series of time delays τ covering about one period of the slow $7f$ oscillation. The two central frames show the entire time series as angle-resolved spectra integrated over the energy window of the probe or reference signal. Green frames in the top row display 3D PMDs for selected time delays covering about one period of the fast $8f$ oscillation. Orange frames in the bottom row display selected 3D PMDs from the $7f$ oscillation. The z projections shown in the background are normalized independently. (b) Calculated 2D sections through the polarization plane of the photoelectron density of the generic Rydberg model (cf. Fig. 2). The snapshots illustrate the yield variation and rotational dynamics of the total density as a result of the intertwined motion of the counterrotating $7f$ and $8f$ crescents, indicated by orange and green arrows.

superposition of the torus-shaped symmetric part and the crescent-shaped antisymmetric part) its effective shape is an unbalanced torus. This asymmetric shape is also visible in the z projections of the 3D graphs. The 3D photoelectron crescent emerges in the isosurface representations. To increase the contrast of the crescent versus the torus in the 3D representation, the already pronounced c_1 Fourier component has been enhanced by a factor of 4 [60]. This enhancement effectively reduces the noise floor in addition. Combined with a spectral low-pass filter applied during the tomographic reconstruction procedure, this results in very smooth surface structures.

The angle-resolved spectra reveal that the PMD undergoes complex dynamics with respect to both the total yield and the angular distribution. To motivate the discussion of these dynamics, we start by analyzing the time evolution of the generic photoelectron crescent in the generic Rydberg model (cf. Fig. 2). For this purpose, Fig. 7(b) presents calculated x-y sections (polarization plane) of the total photoelectron density $\varrho(\boldsymbol{k};\tau)$, showing sequential snapshots of the dynamics. The 2D images display the photoelectron crescent with varying amplitude and orientation. These variations result from the intertwined motion of the $7f$ and $8f$ crescent counterrotating in the polarization plane. When viewed in the $+z$ direction, the $7f$ crescent rotates counterclockwise ($\varpi_{7f} < 0$), while the $8f$ crescent rotates clockwise ($\varpi_{8f} > 0$). Because of their different angular velocities, both crescents periodically shift in-phase (constructive interference) and antiphase (destructive interference). The three columns in Fig. 7(b), labeled by roman numbers I–III, show three consecutive time windows of constructive interference, separated by the instants of maximum destructive interference (dashed gray frames). In each time window, the angular dynamics of the density is governed by the fast clockwise rotation of the $8f$ crescent. This motion is indicated by green arrows. The very first frame shows the onset of constructive interference where the $8f$ crescent starts to shift in-phase with the $7f$ crescent. In the second frame, both crescents are perfectly aligned, resulting in the maximum amplitude and clockwise rotation of the total density. The latter is due to the greater (absolute) angular velocity of the $8f$ crescent. The third frame shows the dephasing of both crescents reducing the signal amplitude but maintaining the rotational sense. In contrast, the slow counterclockwise rotation of the $7f$ crescent is uncovered by comparing similar stages within different time windows of constructive interference, i.e., by comparing different images within one row. For example, upon rephasing and alignment of both crescents (bold black frames) in the second and third time windows, the total density is successively rotated counterclockwise due to the intermediate time evolution of the $7f$ crescent. This motion is indicated by orange arrows. The oscillation period T_{8f} of the $8f$ crescent roughly corresponds to the duration of one time window of constructive interference. The oscillation period T_{7f} of the $7f$ crescent is not complete before the orientation of the crescent at the stage of, for example, maximum amplitude (constructive interference) has performed a full counterclockwise rotation.

In the measured photoelectron spectra, depicted in Fig. 7(a), we also observe alternating time windows of constructive and destructive interference. In each window of constructive interference, the maximum of the PMD appears at a different angle, indicating the rotation of the crescent. Inspecting the simulation, we see that the time windows of constructive interference correspond to tilted ellipses in the 2D representation. The ellipses are separated by valleys of destructive interference and shift successively in the positive angular direction for increasing time delays $|\tau|$ (right to left). This gradual descent of the ellipses indicates the motion of the slowly rotating $7f$ crescent, intersected periodically by destructive interference with the fast rotating $8f$ crescent. Viewed in the $+z$ direction, the negative ϕ shift implies counterclockwise rotation of the $7f$ crescent, in accordance with the negative detuning $\varpi_{7f} < 0$. The angular velocity of the rotation is obtained by evaluation of the orange gradient triangle. In the time interval $\Delta\tau = 65.0$ fs between two recurrences, the ellipses shift by an angle of $\Delta\phi_{7f} = -0.87$ mrad, from which we infer the angular frequency $\varpi_{7f} = \Delta\phi_{7f}/\Delta\tau = -13.4$ mrad/fs. This frequency corresponds to an oscillation period of $T_{7f} = 469$ fs, in good agreement with the above results. The slow rotation is visualized by the measured PMDs in the bottom row (orange frames) of Fig. 7(a). As demonstrated by the PMDs measured for $\tau = -250$ and -700 fs, we observe a recurrence of the crescent shape and orientation (around $\phi = \pi/4$) after approximately a period of T_{7f}. Intermediately, the measured crescent appears to move irregularly, due to the interfering fast rotation of the $8f$ crescent which is not fully resolved in the coarse-grained measurement. To identify the fast $8f$ oscillation in the simulated 2D map, we first notice that the ellipses are tilted in the $+\phi$ direction. This indicates the clockwise rotation of the $8f$ crescent. The magnitude of the slope, however, is not suitable to extract the velocity of the rotation because it is additionally influenced by the beating of the symmetric part. To determine the angular velocity of the $8f$ crescent, we consider that in the recurrence time $\Delta\tau = 65.0$ fs, in which the $7f$ crescent rotates by $\Delta\phi_{7f}$, the $8f$ crescent rotates by $\Delta\phi_{8f} = \Delta\phi_{7f} + 2\pi = 5.41$ rad. Thus we obtain the angular frequency $\varpi_{8f} = \Delta\phi_{8f}/\Delta\tau = 84.0$ mrad/fs. The corresponding oscillation period of $T_{8f} = 74.8$ fs is also in good agreement with the above results. In the figure, the fast $8f$ rotation is indicated by a green gradient triangle, the evaluation of which leads to the same result. Despite the sparsely sampled fast oscillation, the rotation of the $8f$ crescent is captured in the time window between $\tau = -500$ and -575 fs. The corresponding PMDs are shown in the top row (green frames) of Fig. 7(a). Over the period of approximately T_{8f}, the crescent rotates monotonically in a clockwise manner (for increasing $|\tau|$, when viewed in the $+z$ direction) and eventually reproduces its initial orientation (around $\phi = 3\pi/4$).

IV. CONCLUSION AND OUTLOOK

In this paper we presented a shaper-based experimental technique for the time-resolved holographic imaging of ultrafast quantum dynamics. The technique combines CEP-stable bichromatic white light polarization shaping with the tomographic reconstruction of photoelectron wave packets. The physical scheme is based on the CEP-sensitive interference of a probe wave packet from bichromatic $N+1$ REMPI involving the target states and a reference wave packet from single-color $M+1$ MPI of the ground state. The wave packets are created by shaper-generated bichromatic pump-probe pulse sequences with commensurable central frequencies $N\omega_{pu} = M\omega_{pr}$. The red band serves as a pump pulse, initiating the bound-state dynamics via N-photon excitation. The blue band acts as both a probe and a reference pulse, simultaneously ionizing the system from the target states and from the ground state. The former maps the dynamics into the probe wave packet, while the latter provides the reference wave packet for holographic measurements.

To demonstrate the technique, we studied femtosecond Rydberg wave-packet dynamics in K atoms as a model system, employing COCP (2ω:3ω) pulse sequences. The interference of wave packets with different angular momenta yields a highly asymmetric crescent-shaped PMD. The orientation of the crescent in the laser polarization plane is controlled by an interplay of the optical phases, e.g., the CEP, and the quantum phase accumulated between excitation and probe or reference ionization. For fixed optical phase, the rotating crescent represents a pointer indicating quantum phases by virtue of its rotation angle. The use of energy- and angle-resolved detection techniques enables us to disentangle the photoelectron asymmetry from the symmetric dynamical background. In the experiment, the decomposition of the measured PMD into symmetric and antisymmetric parts is achieved by utilizing the CEP sensitivity of the photoelectron asymmetry. Both parts deliver complementary spectroscopic information. The symmetric signal provides information on the beating between pairs of excited Rydberg states, i.e., on the Rydberg beating modes ω_{nm}. Since these are difference frequencies, ambiguities may arise in their spectroscopic assignment. Especially when more than one Rydberg series is excited, e.g., by the use of a linearly polarized pump pulse [32], different modes can be very similar or even indistinguishable. However, the joint analysis of the symmetric and the antisymmetric signal provides unambiguous information on the individual quantum states contributing to the Rydberg dynamics. Moreover, the experimental access to the antisymmetric signal allows for the background-free observation of the crescent dynamics, offering enhanced contrast of the holographic technique. We presented tomographic reconstructions of the 3D PMD for a series of pump-probe time delays. The 3D mapping highlights the crescent shape of the total photoelectron density and illustrates its rotational motion as a phase-sensitive indicator of the bound-electron dynamics.

Time-resolved holographic imaging of the rotating photoelectron crescent yields detailed spectroscopic information on the underlying quantum dynamics. The key to the creation and observation of the crescent is the combination of CEP-sensitive $N+1$ vs $M+1$ REMPI with the highly differential detection of the released photoelectron wave packets. Currently, we employ the holographic technique to investigate resonance-induced phase dynamics in the perturbative multiphoton excitation or ionization of atomic model systems. For this purpose, we use the shaper to vary the central wavelengths of pump and probe, while keeping the bichromatic ratio fixed, and compare the results for resonant and off-resonant

multiphoton excitation. In addition, we study intensity-dependent phase shifts due to, for example, the resonant (Autler-Townes) and nonresonant AC Stark effect in nonperturbative laser-atom interactions. Such effects are not accounted for in the theoretical description presented in Sec. II A, but are included in our numerical simulations.

Owing to the shaper-based approach, the presented technique is robust, tunable, and highly versatile, holding great promise for holographic investigations of ultrafast dynamics in more complex quantum systems such as multielectron atoms, polyatomic molecules, and nanometric structures.

ACKNOWLEDGMENT

Financial support from the Deutsche Forschungsgemeinschaft via the priority program QUTIF (Program No. SPP1840) is gratefully acknowledged.

[1] C. Leichtle, W. P. Schleich, I. S. Averbukh, and M. Shapiro, Phys. Rev. Lett. **80**, 1418 (1998).
[2] F. Krasniqi, B. Najjari, L. Struder, D. Rolles, A. Voitkiv, and J. Ullrich, Phys. Rev. A **81**, 033411 (2010).
[3] J. Mauritsson, T. Remetter, M. Swoboda, K. Klünder, A. L'Huillier, K. J. Schafer, O. Ghafur, F. Kelkensberg, W. Siu, P. Johnsson, M. J. J. Vrakking, I. Znakovskaya, T. Uphues, S. Zherebtsov, M. F. Kling, F. Lepine, E. Benedetti, F. Ferrari, G. Sansone, and M. Nisoli, Phys. Rev. Lett. **105**, 053001 (2010).
[4] D. M. Villeneuve, P. Hockett, M. J. J. Vrakking, and H. Niikura, Science **356**, 1150 (2017).
[5] G. Porat, G. Alon, S. Rozen, O. Pedatzur, M. Krüger, D. Azoury, A. Natan, G. Orenstein, B. D. Bruner, M. J. J. Vrakking, and N. Dudovich, Nat. Commun. **9**, 2805 (2018).
[6] J. F. Christian, L. C. Snoek, S. G. Clement, and W. J. van der Zande, Phys. Rev. A **53**, 1894 (1996).
[7] D. W. Schumacher, J. H. Hoogenraad, D. Pinkos, and P. H. Bucksbaum, Phys. Rev. A **52**, 4719 (1995).
[8] T. Remetter, P. Johnsson, J. Mauritsson, K. Varju, Y. Ni, F. Lepine, E. Gustafsson, M. Kling, J. Khan, R. Lopez-Martens, K. J. Schafer, M. J. J. Vrakking, and A. L'Huillier, Nat. Phys. **2**, 323 (2006).
[9] P. F. Tekavec, T. R. Dyke, and A. H. Marcus, J. Chem. Phys. **125**, 194303 (2006).
[10] J. A. Cina, Annu. Rev. Phys. Chem. **59**, 319 (2008).
[11] K. Ohmori, Annu. Rev. Phys. Chem. **60**, 487 (2009).
[12] J. J. Barton, Phys. Rev. Lett. **61**, 1356 (1988).
[13] T. C. Weinacht, J. Ahn, and P. H. Bucksbaum, Phys. Rev. Lett. **80**, 5508 (1998).
[14] A. Monmayrant, B. Chatel, and B. Girard, Opt. Commun. **264**, 256 (2006).
[15] X. B. Bian and A. D. Bandrauk, Phys. Rev. Lett. **108**, 263003 (2012).
[16] D. Gábor, Science **177**, 299 (1972).
[17] D. Gábor, in *Nobel Lectures in Physics 1971–1980*, edited by S. Lundqvist (World Scientific, Singapore, 1992).
[18] Y. T. Mazurenko, Appl. Phys. B **50**, 101 (1990).
[19] L. H. Acioli, M. Ulman, E. P. Ippen, J. G. Fujimoto, H. Kong, B. S. Chen, and M. Cronin-Golomb, Opt. Lett. **16**, 1984 (1991).
[20] T. C. Weinacht, J. Ahn, and P. H. Bucksbaum, Nature (London) **397**, 233 (1999).
[21] Y. Huismans, A. Rouzée, A. Gijsbertsen, J. H. Jungmann, A. S. Smolkowska, P. Logman, F. Lepine, C. Cauchy, S. Zamith, and T. Marchenko, Science **331**, 61 (2011).
[22] K. Klünder, P. Johnsson, M. Swoboda, A. L'Huillier, G. Sansone, M. Nisoli, M. J. J. Vrakking, K. J. Schafer, and J. Mauritsson, Phys. Rev. A **88**, 033404 (2013).
[23] M. Meckel, A. Staudte, S. Patchkovskii, D. M. Villeneuve, P. B. Corkum, R. Dorner, and M. Spanner, Nat. Phys. **10**, 594 (2014).
[24] M. Wollenhaupt, C. Lux, M. Krug, and T. Baumert, Chem. Phys. Chem. **14**, 1341 (2013).
[25] S. Kerbstadt, D. Pengel, D. Johannmeyer, L. Englert, T. Bayer, and M. Wollenhaupt, New J. Phys. **19**, 103017 (2017).
[26] S. Kerbstadt, D. Pengel, L. Englert, T. Bayer, and M. Wollenhaupt, Phys. Rev. A **97**, 063402 (2018).
[27] S. Kerbstadt, K. Eickhoff, T. Bayer, and M. Wollenhaupt, Nat. Commun. **10**, 658 (2019).
[28] S. Kerbstadt, L. Englert, T. Bayer, and M. Wollenhaupt, J. Mod. Opt. **64**, 1010 (2017).
[29] S. Kerbstadt, D. Timmer, L. Englert, T. Bayer, and M. Wollenhaupt, Opt. Express **25**, 12518 (2017).
[30] A. N. Pfeiffer, C. Cirelli, M. Smolarski, and U. Keller, Chem. Phys. **414**, 84 (2013).
[31] T. Bayer, D. Gräfing, S. Kerbstadt, D. Pengel, K. Eickhoff, L. Englert, and M. Wollenhaupt, New J. Phys. **21**, 033001 (2019).
[32] S. Kerbstadt, L. Gabrisch, K. Eickhoff, T. Bayer, and M. Wollenhaupt, Phys. Rev. A **99**, 013406 (2019).
[33] I. S. Averbukh, M. Shapiro, C. Leichtle, and W. P. Schleich, Phys. Rev. A **59**, 2163 (1999).
[34] T. Brixner and G. Gerber, Opt. Lett. **26**, 557 (2001).
[35] A. M. Weiner, Opt. Commun. **284**, 3669 (2011).
[36] A. Präkelt, M. Wollenhaupt, C. Sarpe-Tudoran, and T. Baumert, Phys. Rev. A **70**, 063407 (2004).
[37] J. I. Steinfeld, *Molecules and Radiation: An Introduction to Modern Molecular Spectroscopy* (Courier, Chelmsford, 2012).
[38] D. Meshulach and Y. Silberberg, Phys. Rev. A **60**, 1287 (1999).
[39] A. Gandman, L. Chuntonov, L. Rybak, and Z. Amitay, Phys. Rev. A **75**, 031401(R) (2007).
[40] M. Wollenhaupt, M. Krug, J. Köhler, T. Bayer, C. Sarpe-Tudoran, and T. Baumert, Appl. Phys. B **95**, 245 (2009).
[41] M. Abel, D. M. Neumark, S. R. Leone, and T. Pfeifer, Laser Photon. Rev. **5**, 352 (2011).
[42] G. Cerullo, A. Baltuska, O. D. Mucke, and C. Vozzi, Laser Photon. Rev. **5**, 323 (2011).
[43] B. H. Bransden and C. J. Joachain, in *Physics of Atoms and Molecules*, 2nd ed. (Pearson Education, London, 2003), p. 1114.
[44] C. Meier and V. Engel, Phys. Rev. Lett. **73**, 3207 (1994).
[45] P. Eckle, M. Smolarski, P. Schlup, J. Biegert, A. Staudte, M. Schöffler, H. G. Muller, R. Dörner, and U. Keller, Nat. Phys. **4**, 565 (2008).
[46] J. Parker and C. R. Stroud, Phys. Rev. Lett. **56**, 716 (1986).
[47] G. Alber, H. Ritsch, and P. Zoller, Phys. Rev. A **34**, 1058 (1986).
[48] L. D. Noordam and R. R. Jones, J. Mod. Opt. **44**, 2515 (1997).

[49] B. Whitaker, in *Imaging in Molecular Dynamics*, 1st ed. (Cambridge University Press, Cambridge, 2003), p. 249.

[50] R. Bracewell, *The Fourier Transform and its Applications* (McGraw-Hill Higher Education, Singapore, 2000), Vol. 3.

[51] A. T. J. B. Eppink and D. H. Parker, Rev. Sci. Instrum. **68**, 3477 (1997).

[52] M. Wollenhaupt, M. Krug, J. Köhler, T. Bayer, C. Sarpe-Tudoran, and T. Baumert, Appl. Phys. B **95**, 647 (2009).

[53] J. Köhler, M. Wollenhaupt, T. Bayer, C. Sarpe, and T. Baumert, Opt. Express **19**, 11638 (2011).

[54] C. Smeenk, L. Arissian, A. Staude, D. M. Villeneuve, and P. B. Corkum, J. Phys. B **42**, 185402 (2009).

[55] P. Hockett, M. Staniforth, and K. L. Reid, Mol. Phys. **108**, 1045 (2010).

[56] J. Maurer, D. Dimitrovski, L. Christensen, L. B. Madsen, and H. Stapelfeldt, Phys. Rev. Lett. **109**, 123001 (2012).

[57] C. Chen, Z. Tao, C. Hernández-García, P. Matyba, A. Carr, R. Knut, O. Kfir, D. Zusin, C. Gentry, P. Grychtol, O. Cohen, L. Plaja, A. Becker, A. Jaron-Becker, H. Kapteyn, and M. Murnane, Sci. Adv. **2**, e1501333 (2016).

[58] A. C. Kak and M. Slaney, in *Principles of Computerized Tomographic Imaging* (IEEE, New York, 1988), pp. 1–339.

[59] A. Kramida, Y. Rachenko, and J. Reader, *Atomic Spectra Database* (National Institute of Standards and Technology, Gaithersburg, 2018), available at https://www.nist.gov/pml/atomic-spectra-database.

[60] D. Pengel, S. Kerbstadt, L. Englert, T. Bayer, and M. Wollenhaupt, Phys. Rev. A **96**, 043426 (2017).